

Electronic Supplementary Information (ESI)

Ambient Rutile VO₂(R) Hollow Hierarchitectures with Rich Grain Boundaries from New-State Nsutite-Type VO₂, Displaying Enhanced Hydrogen Adsorption Behavior

By Junfeng Xie, Changzheng Wu*, Shuanglin Hu, Jun Dai, Ning Zhang, Jun Feng, Jinlong Yang and Yi Xie*

E-mail: czwu@ustc.edu.cn; yxie@ustc.edu.cn.

Table of contents

- S1.** Shape evolution of the new-state VO₂ hollow spherical nanoarchitectures
- S2.** Compositional characterization of the new-state nsutite-type VO₂ precursor
- S3.** Summary XRD patterns of the nsutite-type VO₂ prepared by different chemical reactions
- S4.** Structural determination of new-state VO₂
- S5.** Calculation details and phase conversion process from the new-state nsutite-type VO₂ to rutile VO₂(R)
- S6.** Characterization of the GBR-VO₂(R) hollow hierarchitectures
- S7.** Gas adsorption experiments of different vanadium oxides

References in Electronic Supplementary Information

S1. Shape evolution of the new-state VO₂ hollow spherical nanoarchitectures

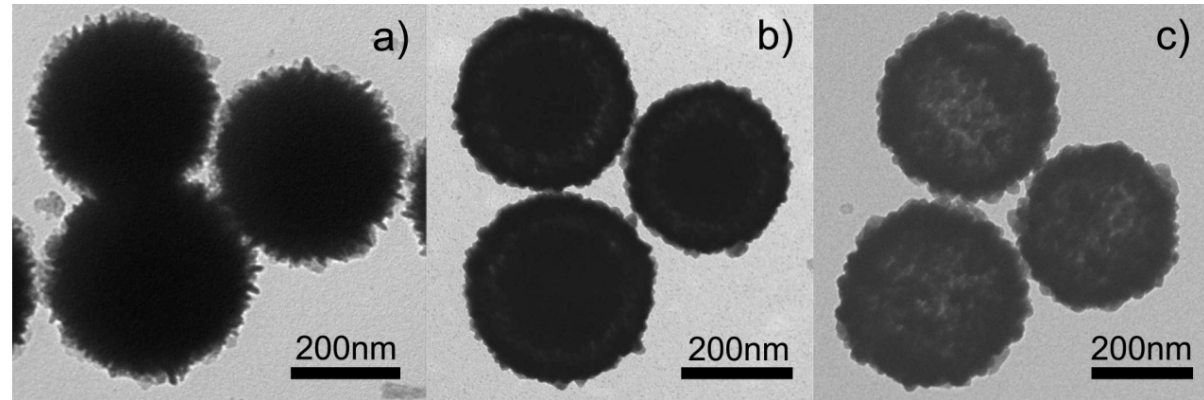


Figure S1. Time-dependent experiments of the formation mechanism of the new-phased vanadium dioxide carried out at 180 °C. a) Solid sphere structures were obtained at 2 h. b) Core/shell structures at 6 h. c) the monodispersed hollow spherical nanoarchitectures of the new-phased vanadium dioxide after reacting for 24 h. The formation process is following the well-known Ostwald ripening mechanism.

S2. Composition of the new-state nsutite-type VO₂ precursor

S2-1. Energy-dispersive X-ray Spectra (EDX) of the new-state nsutite-type VO₂ precursor

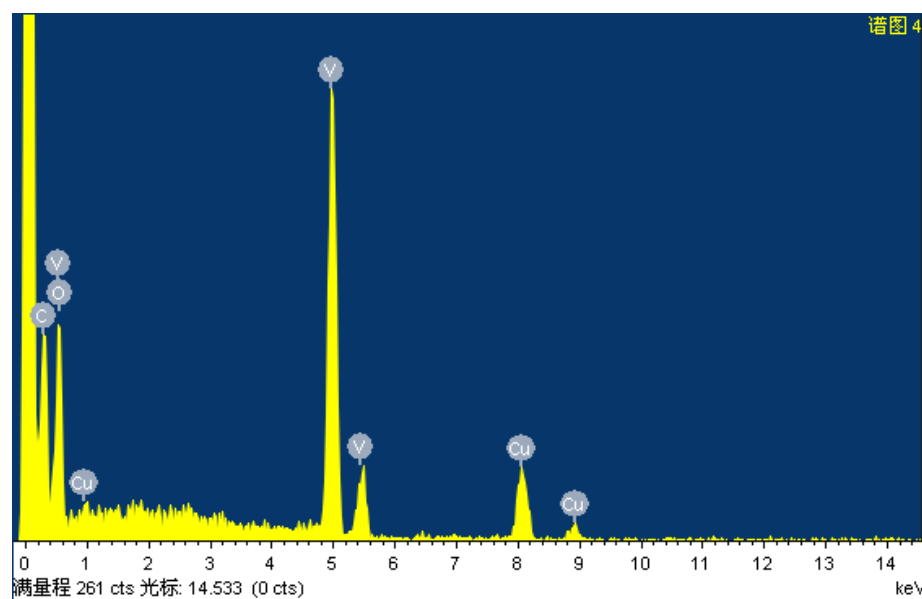


Figure S2. Energy-dispersive X-ray spectra (EDX) reveals that the product is composed of only V and O, and no other elements are detected. Of note, copper and carbon signals arise from the TEM grid. However, the atom ratio of V and O cannot be determined because one peak for the element V overlaps with the peak of O.

S2-2. X-ray photoelectron spectroscopy (XPS) spectra of the new-state nsutite-type VO_2 precursor

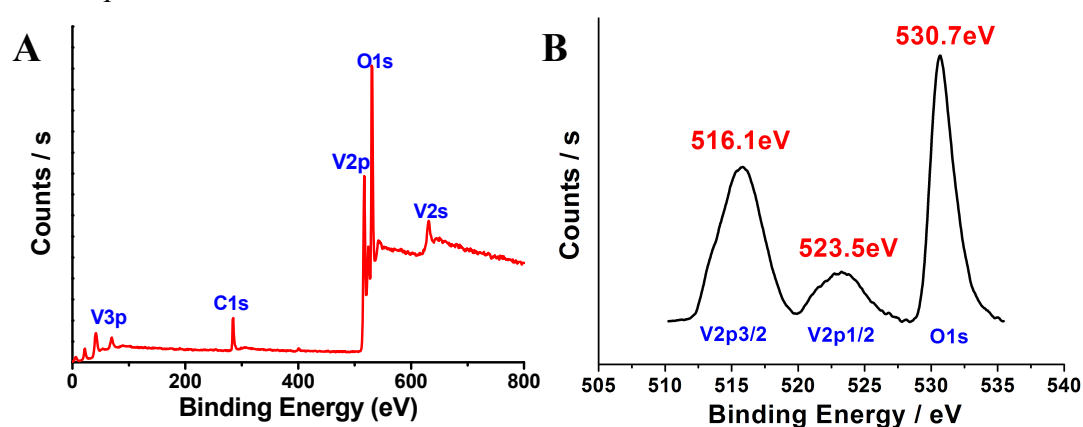


Figure S3. (A) XPS survey spectra of the nsutite-type VO_2 . (B) High-resolution XPS (HR-XPS) spectra of the nsutite-type VO_2 after removing the background.

S2-3. Thermogravimetric analysis (TGA) and XRD patterns of different stages in the heating process

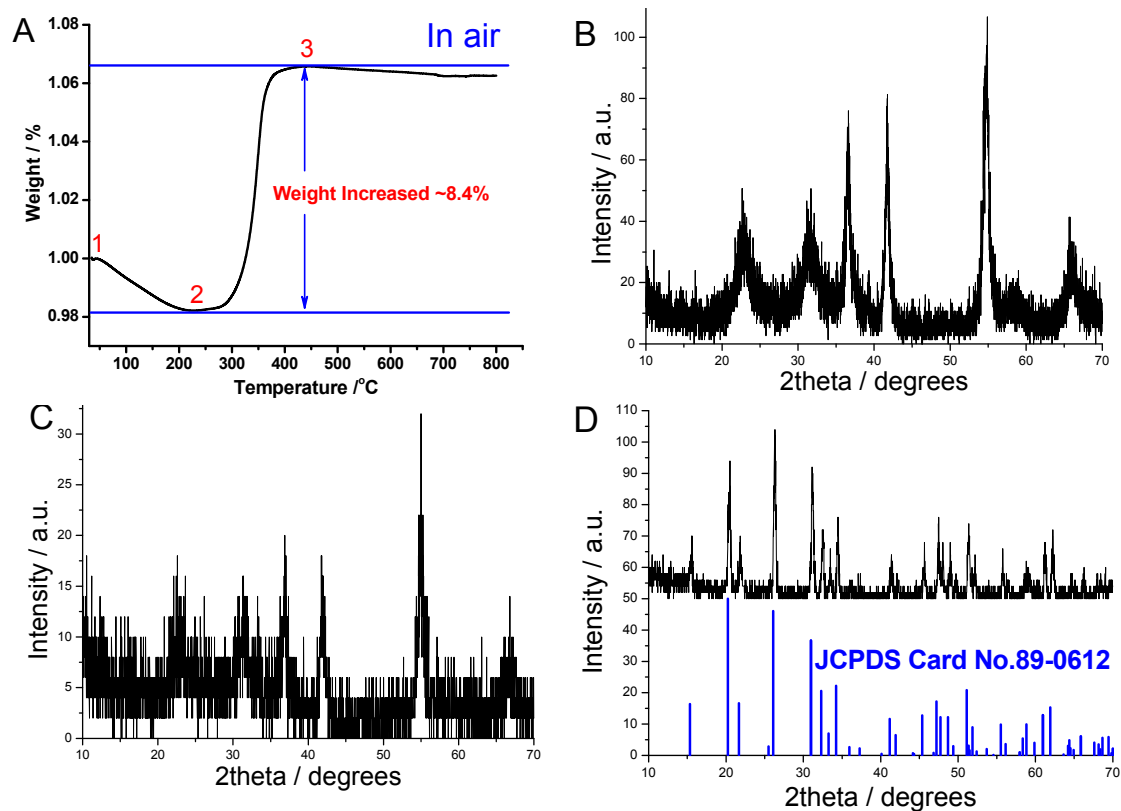


Figure S4. (A) Thermogravimetric analysis (TGA) curve measured under air atmosphere with temperature ranging from room temperature to 800 °C. XRD patterns as shown in Figure S4 B, C and D of the intermediate samples corresponds to the different stages as noted by 1, 2, 3 in Figure S4A, respectively. The XRD patterns show that the sample heating in air at 200 °C still maintains nsutite-type state. When the temperature is elevated to 400 °C, the higher oxidization state of $\text{V}(\text{V})_2\text{O}_5$ is formed.

S3. Summary XRD patterns of the nsutite-type vanadium dioxides prepared by different chemical reaction routes

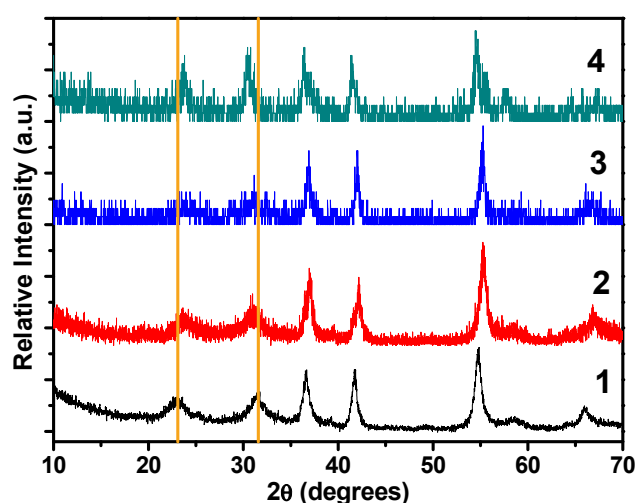


Figure S5. XRD patterns of the nsutite-type vanadium dioxides prepared by different routes.

Of note, the two peaks with 2θ values of ~ 22° and ~ 35° were indeed shifted in different samples (Figure S5), and the 2θ value gap between these two peaks reflects the concentration value of single/double chains (i.e. P_r or P_R) dependent of the prepared sample characteristics. These features can be well illustrated by the De Wolff model, and also provides the auxilliary evidence for the verification of using De Wolff model to illustrate the new-state vanadium oxides in our cases.

Preparation details of four nsutite-type vanadium dioxides:

1. As-prepared nsutite-type VO₂ hollow spherical nanoarchitectures in this article.
2. 0.03 g paramontroseite VO₂(P) was added to a mixture of 28 mL deionized water and 2 mL tetrahydrofuran (THF) and stirred for several minutes, then the suspension was transferred into a 35 mL Teflon-lined stainless steel autoclave and heated at 220 °C for 3 days. The as-obtained products was washed with deionized water and absolute ethanol, and dried at 60 °C under vacuum.
3. 0.1085 g VOSO₄·xH₂O was dissolved in 40 mL deionized water and 1 mL 1M H₃PO₄ was injected, then 0.135 g NaOH was added into the solution. After several minutes' stirring, the mixture was transferred into a 50 mL Teflon-lined stainless steel autoclave and heated at 220 °C for 18 hours. The as-obtained products was washed with deionized water and absolute ethanol, and dried at 60 °C under vacuum.
4. 2 mmol NH₄VO₃ were loaded into a jar containing 45 ml distilled water and the turbid solution was strongly stirred for 10 min. Then 1 mL 1 M HCl solution was slowly added dropwise into the solution, ensuring the system to be a transparent yellow solution. After the given amount of N₂H₄·H₂O (3 ml, 80%) was introduced into the prepared solution and strongly stirred for 30 min at the room temperature, the solid precursor of V(OH)₂NH₂ were obtained when the homogeneous solution turned to be turbid and its color evolved from yellow to gray. The V(OH)₂NH₂ sample was then collected by centrifugation for following experiments. The collected V(OH)₂NH₂ sample as described above was further ultrasonically dispersed in 30 ml distilled water, and then 2.5 ml 0.1M HNO₃ solution was added dropwise. After strongly stirring, the V(OH)₂NH₂ suspension solution was sealed in a 40 ml autoclave and heated at the

temperature of 200 °C for 36 h. The system was then allowed to cool to room temperature. The final VO₂(M) sample was collected by centrifugation, and washed with deionized water to remove any possible ionic remnants, then dried in a vacuum at 50 °C.

S4. Structural determination of new-state VO₂

S4-1. Structural information of new-state VO₂ from the detailed analysis of the XRD patterns

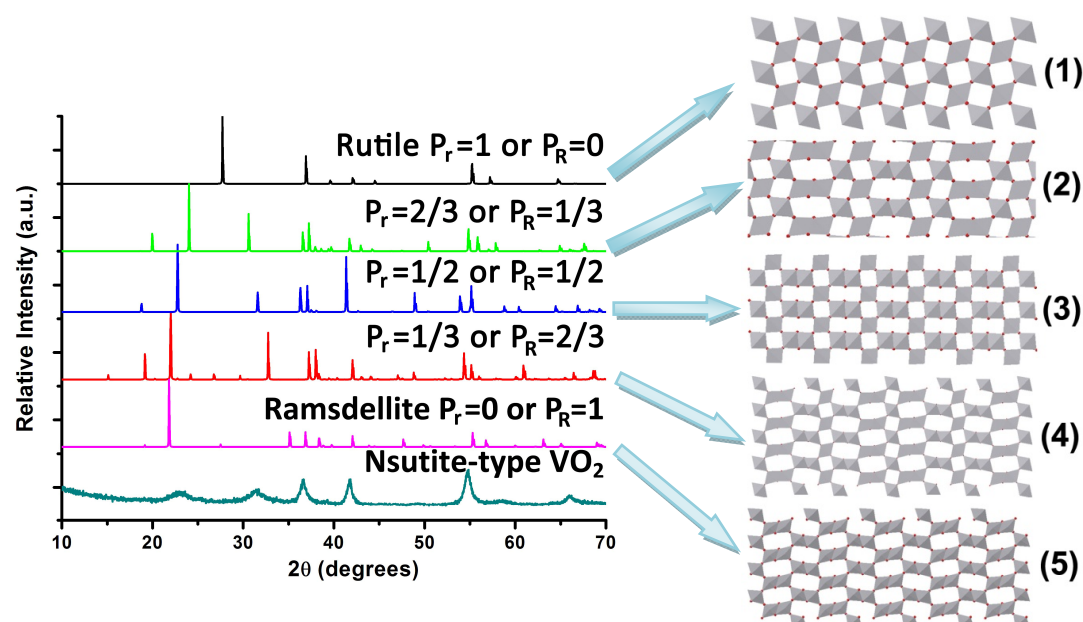


Figure S6. XRD patterns of VO₂ structures with different P_r values according to well-known De Wolff model. The top five XRD patterns were plotted by calculated data from five different structure models of De Wolff model on the right, with P_r=1, 2/3, 1/2, 1/3, 0 or P_R=0, 1/3, 1/2, 2/3, 1 from top to bottom, respectively.

The corresponding X-ray powder diffraction (XRD) pattern provides further structural information of the as-obtained VO₂ product. The XRD pattern (bottom) of the as-obtained vanadium dioxide hollow spherical nanoarchitectures are always of rather poor quality and consist, at best, of a small number of sharp and broad lines on top of a diffuse background. Moreover, the XRD pattern couldn't be indexed to any standard XRD patterns in the Powder Diffraction Standards (JCPDS) cards, or previously reported vanadium-including materials, revealing a new kind of material. Careful observation shows that a few peaks match more or less accurately that of rutile phase VO₂(R) while most exhibit a striking resemblance with the diffraction pattern of ramsdellite-type VO₂ (i.e. paramontroseite VO₂(P) in vanadium minerals), the characteristics of which is high resemblance with that of nsutite γ-MnO₂: the XRD pattern of nsutite γ-MnO₂ shows that the poorest pattern consists of a strong diffuse background, in which the greater part of peaks happen to match certain lines of rutile-type pyrolusite MnO₂ and the most line-rich patterns also show a striking resemblance with the pattern of another MnO₂ mineral called ramsdellite, leading to the well-accepted pyrolusite-ramsdellite intergrowth model of nsutite γ-MnO₂. Obviously, our as-obtained vanadium dioxide could also be regarded as the intergrowth of rutile and ramsdellite structure, i.e. De Wolff model. As is known, VO₂(P) possesses a regular tunnel form, in which the

VO_6 octahedra are linked into double chains and the double chains link corners with each other in turn to form a framework having tunnels with rectangular-shaped cross sections that are 1×2 octahedra on a side. In $\text{VO}_2(\text{R})$, all VO_6 octahedra are linked by sharing an edge along the c -axis to form chains, and the chains are then interlinked by sharing corner oxygen atoms to form a 3D framework. The De Wolff model is based on the observation that rutile and ramsdellite structures have similar arrangements along their a and c axes and differ only by the width of the infinite strings of $[\text{MO}_6]$ octahedra along the b axis: single and double chains in rutile and ramsdellite, respectively. We used the same treating method to understand our nsutite-type VO_2 structure, which hypothesis explains the line shifts and broadening observed in X-Ray diffraction patterns, at least for the “line-rich type” nsutite samples. And in our case, the statistical tools are carried out to describe the sequence of the two kinds of layers of rutile with single chains and ramsdellite with double chains. P_r and P_R are the respective fraction of single and double chain slabs in a given sample. For a given intergrowth structure, $P_r + P_R = 1$. We constructed the crystal structure with a gradual evolution of P_r/P_R value based on the De Wolff model. And the corresponding rutile-ramsdellite (i.e. paramontroseite $\text{VO}_2(\text{P})$ in vanadium minerals) intergrowth structure with the different concentration of single (r) (P_r) and double (R) (P_R) chains were shown in the right part. The corresponding simulated XRD patterns of the intergrowth structure were (1), (2), (3), (4) to (5) with $P_r=1, 2/3, 1/2, 1/3, 0$ or $P_R=0, 1/3, 1/2, 2/3, 1$, respectively. The simulated XRD curves with increment of P_r give the clear tendency. As is shown, the two peaks ($2\theta=22^\circ, 35^\circ$) in ramsdellite gradually converged into a single peak in rutile, and the 2θ value gap between these two peaks reflects the concentration value of single/double chains (i.e. P_r or P_R) dependent of the prepared sample characteristics; while for the others the peak positions remain no obvious shifting. From the simulated pattern viewpoint, the as-obtained vanadium dioxide could be readily indexed to the nsutite-type VO_2 with P_r in the range of $1/2\sim 1/3$ or P_R in $1/3\sim 1/2$, having the random intergrowth structure of rutile and ramsdellite-type VO_2 (i.e. paramontroseite $\text{VO}_2(\text{P})$) as a new material state in vanadium dioxides. The broadening peaks and high background of the XRD patterns lies in the presented disordered structure built up by rutile and paramontroseite components.

S4-2. HRTEM image and SAED pattern of new-state nsutite-type VO_2

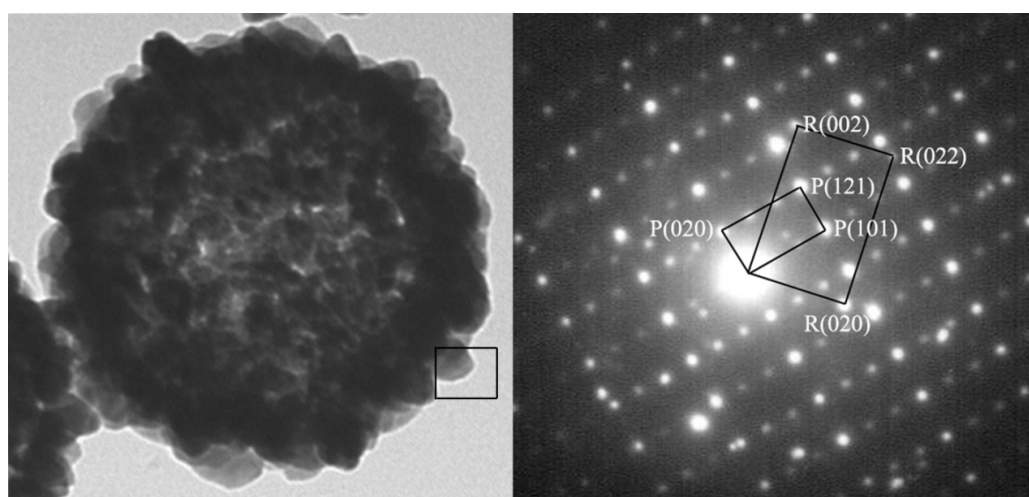


Figure S7. HRTEM image and its SAED pattern on a rice-shaped particle with less grain boundaries on the hollow spherical shell of new-state nsutite-type VO_2 .

The SAED pattern indeed reveals two series of diffraction spots with distinguishable intensity difference. In one serial, the two interplanar spaces of about 4.654 Å and 2.510 Å with the angle value of 90° correspond to the (020) and (101) plane of paramontroseite VO₂; while in another one, the lattice spaces of 1.434 Å and 2.275 Å with the angle value of 90° correspond to the perpendicular (002) and (020) planes of rutile VO₂. The superlattice structure of the as-obtained hollow spheres provides direct evidence for the existence of the intergrowth structure in nsutite-type VO₂.

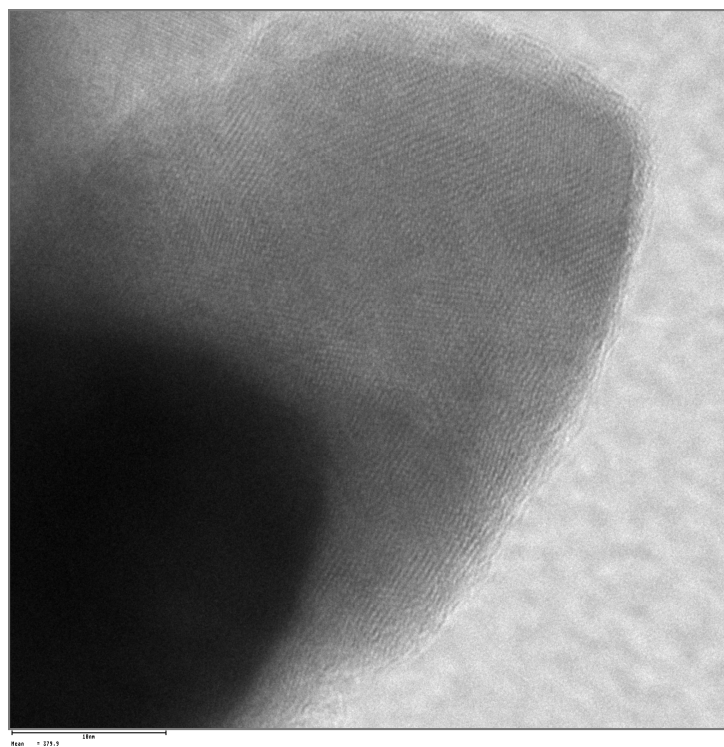


Figure S8. HRTEM image of new-state nsutite-type VO₂ from which we can clearly see the abundant defects such as distortions and dislocations.

S5. Calculation details and phase conversion process from the new-state nsutite-type VO₂ to rutile VO₂(R)

S5-1. Calculation details of different states of the new-state nsutite-type vanadium dioxide model

Calculation details: The electronic structure of different states of the De Wolff model were performed using the projector augmented-wave (PAW) method^[1] with the Perdew-Burke-Ernzerhof (PBE) GGA functional^[2] and Heyd-Scuseria-Ernzerhof (HSE) hybrid functional^[3] as recently implemented in VASP code.^[4-6] The energy cutoff was set to 500 eV. Gamma-centered Monkhorst-Pack k-points sampling method with around 0.04 Å⁻¹ spacings were used for energy calculations. The geometries were relaxed until residual atomic forces less than 0.02 eV/Å with PBE functional, and then the total energies were calculated by both PBE and HSE functionals. The energies per VO₂ unit in each state are thus presented in Table S1.

States	PBE Energy/VO ₂ pair	HSE Energy/VO ₂ pair
	[eV]	[eV]
Rutile VO ₂ (R) (P _r =1)	-25.654	-34.342
P _r =2/3 and P _R =1/3	-25.580	-34.250
P _r =1/2 and P _R =1/2	-25.495	-34.183
P _r =1/3 and P _R =2/3	-25.518	-34.170
Ramsdellite-type VO ₂ (P _R =1)	-25.482	-34.126

Table S1. Perdew-Burke-Ernzerhof (PBE) energy and Heyd-Scuseria-Ernzerhof (HSE) energy of different models of the new-state nsutite-type vanadium dioxide, as well as pure rutile VO₂(R).

S5-2. XRD evolution of heat treatment with the variation of time at 350 °C

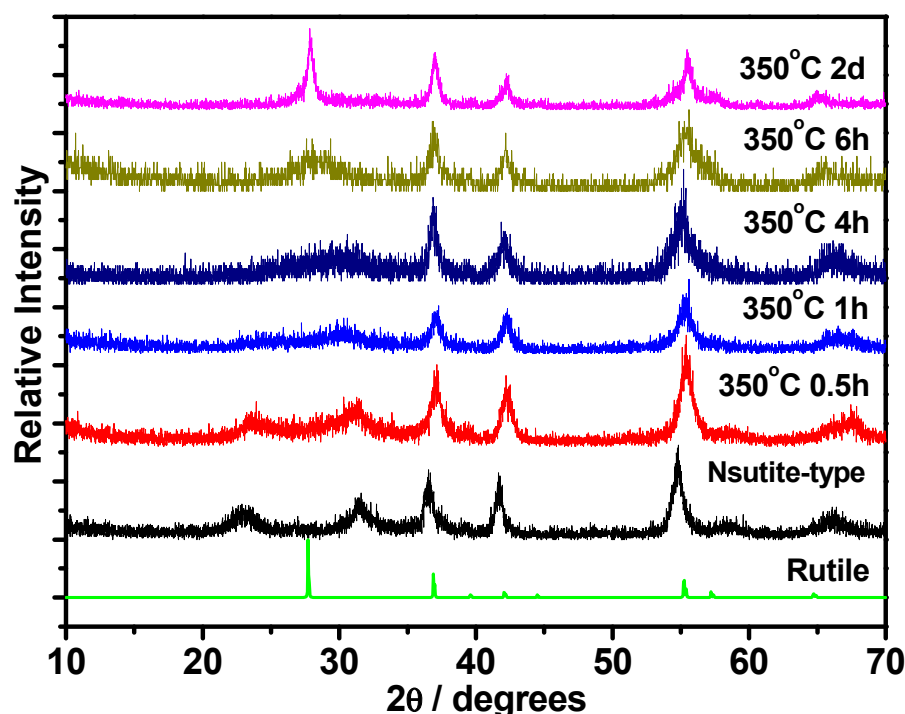


Figure S9. From the calcinations experiments results at different heating durations we realized that the first two broad peaks were integrating gradually with the treating time prolonged and continuous heating can gave VO₂(R) and eventually monoclinic VO₂ with good crystallinity. Note the two broad peaks ($2\theta=22^\circ, 35^\circ$) gradually converged into a single peak in rutile, which is consistent with trend of the De Wolff model we built for the nsutite-type VO₂.

S5-3. Structural transformation from nsutite-type VO_2 model to rutile $VO_2(R)$

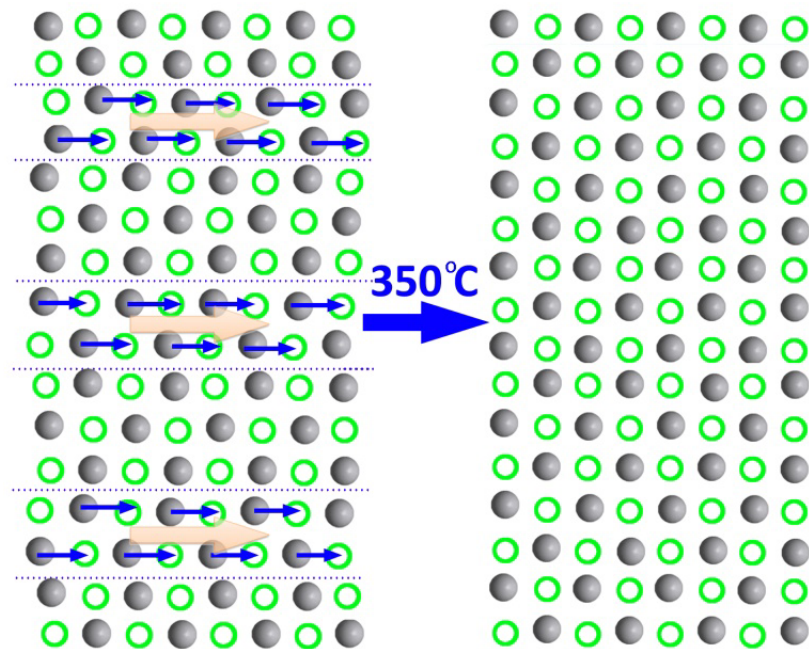


Figure S10. Schematic illustration of the phase conversion from nsutite-type VO_2 to rutile VO_2 in which the structure of the nsutite-type VO_2 is in the form of $P_f=1/3$ or $P_R=2/3$.

S6. Characterization of the GBR- $VO_2(R)$ hollow hierarchitectures

S6-1. Low-resolution SEM image of the as-prepared GBR- $VO_2(R)$ hollow hierarchitectures

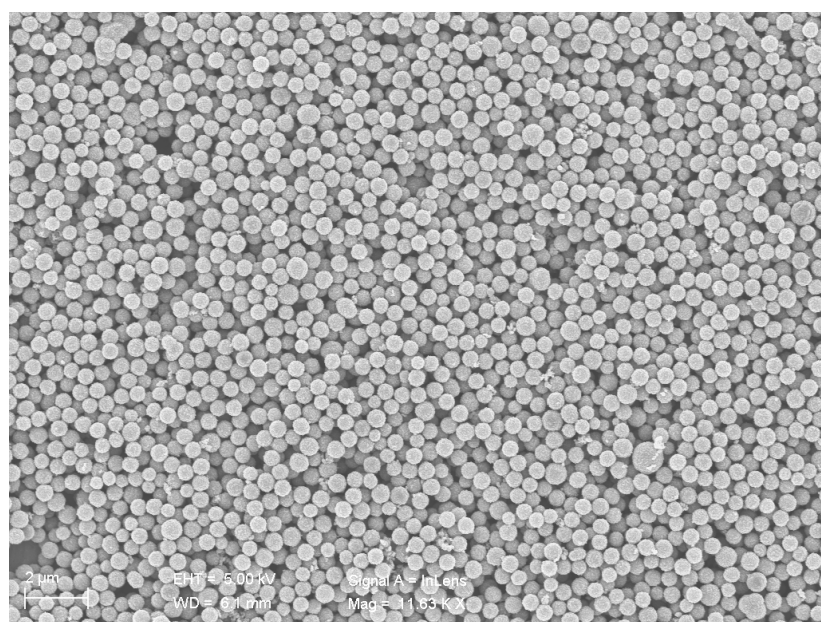


Figure S11. Low-resolution SEM image of the as-prepared GBR- $VO_2(R)$ hollow hierarchitectures revealed that the product after calcination process is of high quantity.

S6-2. Differential scanning calorimeter (DSC) of the GBR-VO₂(R) hollow hierarchitectures

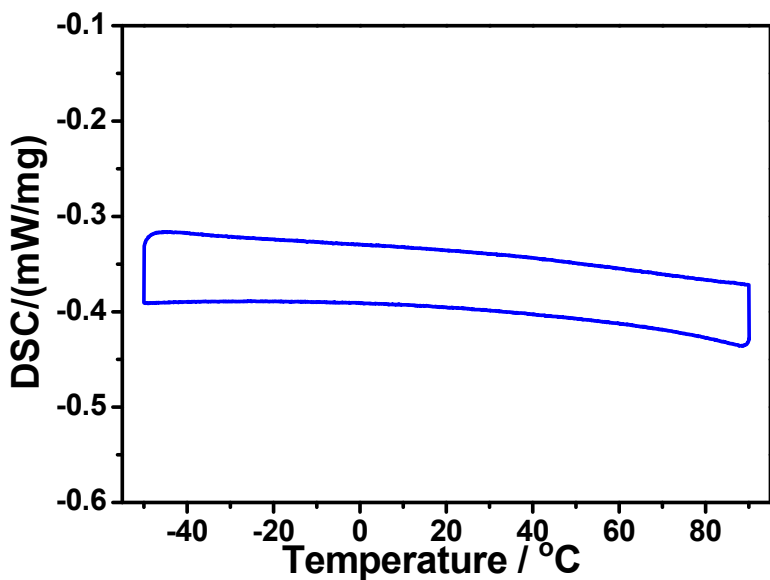


Figure S12. Differential scanning calorimeter (DSC) of the as-obtained rutile VO₂(R) hollow hierarchitectures shows that neither endothermic nor exothermal peak was detected ranging from -50 °C to 100 °C indicating that there were no obvious phase transition in this temperature range and giving the auxiliary evidence for ambient rutile VO₂(R) at room temperature.

S6-3. Fourier transform infrared spectroscopy (FTIR) spectra of paramontroseite VO₂, nsutite-type VO₂ and grain-boundary-rich VO₂(R)

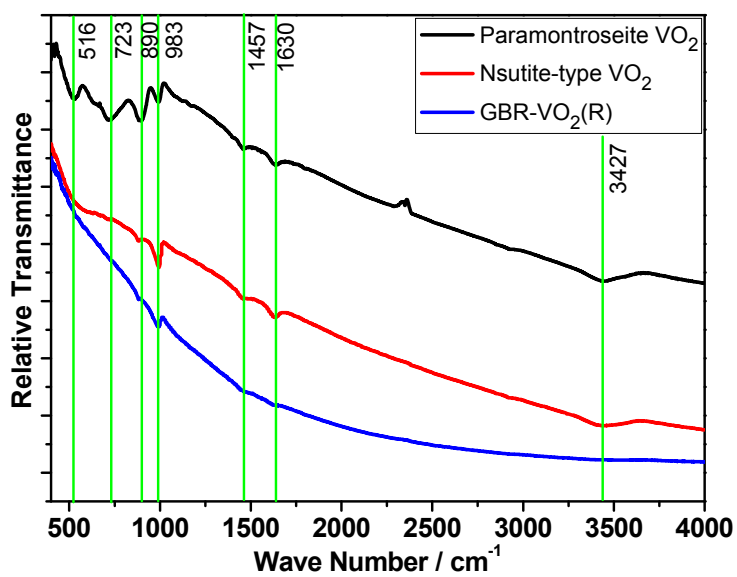


Figure S13. Fourier transform infrared spectroscopy (FTIR) spectra of paramontroseite VO₂, nsutite-type VO₂ and grain-boundary-rich VO₂(R). The broad peaks at 3427 cm⁻¹ could be indexed as -OH signal of adsorbed water exist in paramontroseite VO₂ and nsutite VO₂ except for GBR-VO₂(R).

S7. Gas adsorption experiments of different vanadium oxides

S7-1. N_2 adsorption-desorption measurements of different vanadium oxide samples

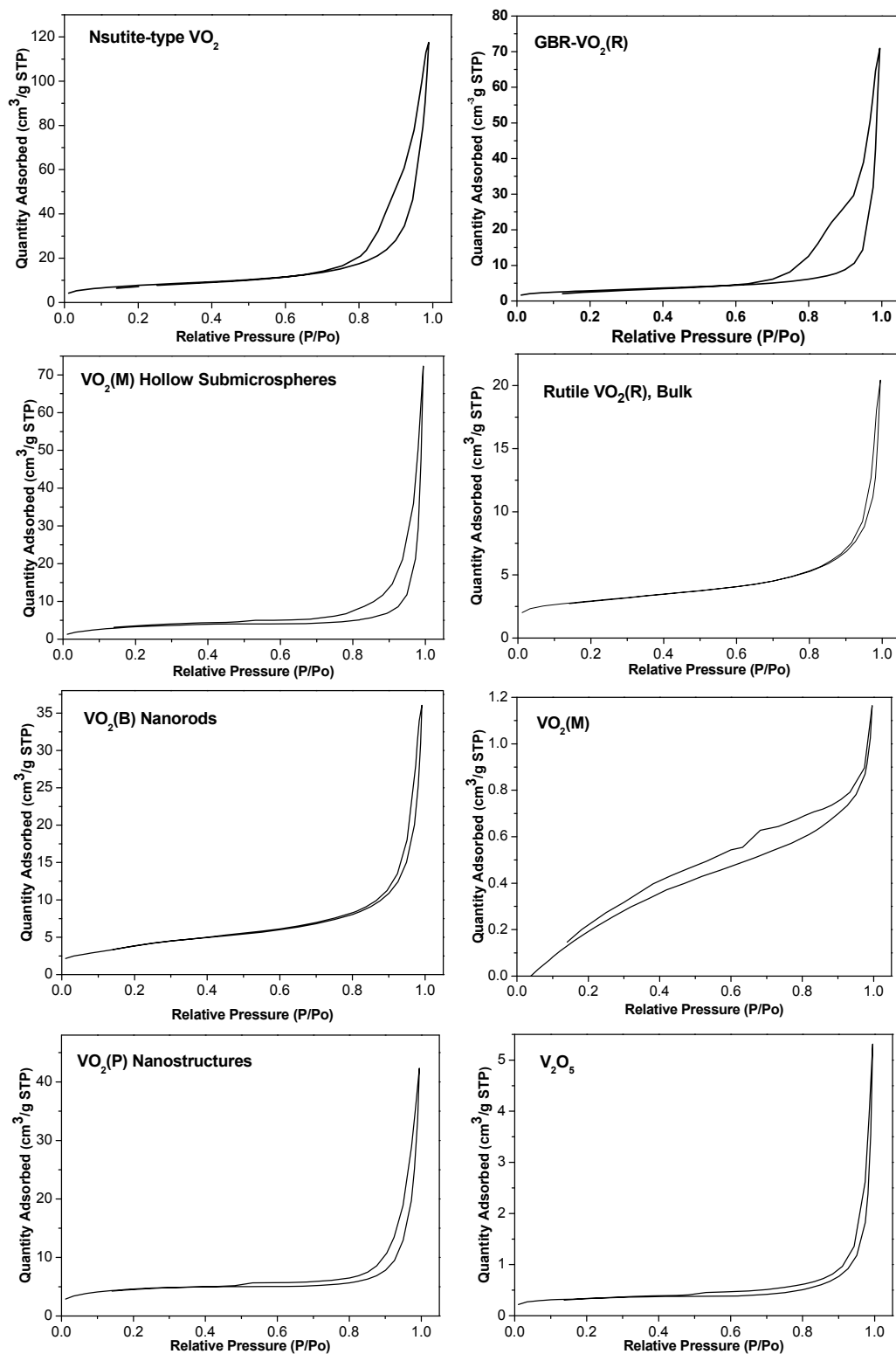


Figure S14. N_2 adsorption-desorption measurements of different vanadium oxide samples.

S7-2. Hydrogen uptake measurements of different vanadium oxide samples

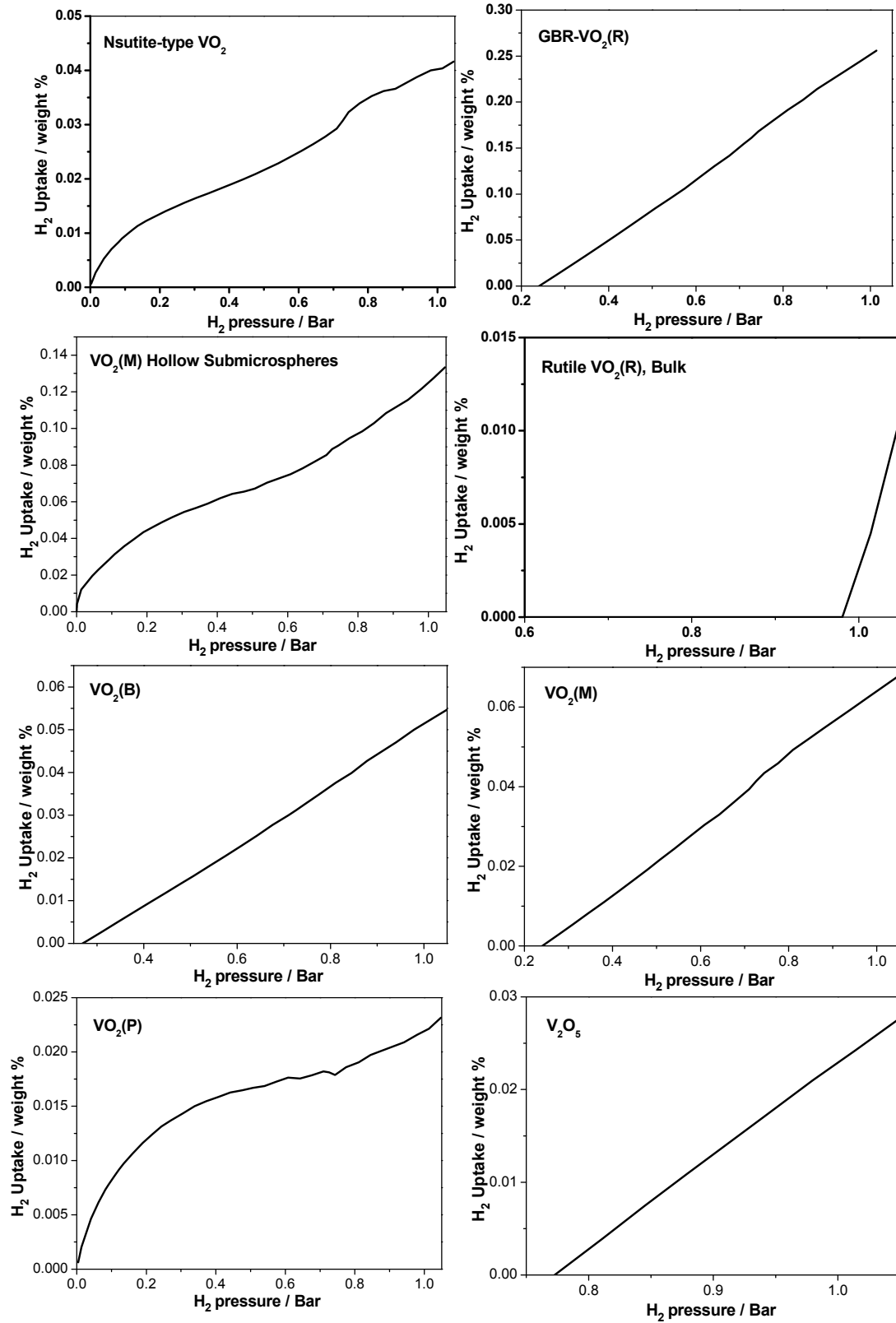


Figure S15. Hydrogen uptake measurements of different vanadium oxide samples.

S7-3. XRD pattern of the monoclinic $\text{VO}_2(\text{M})$ hollow submicrospheres

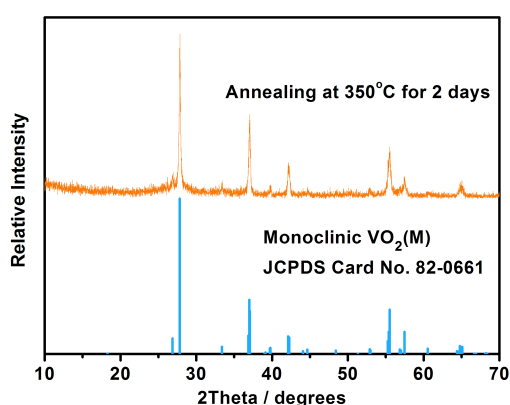


Figure S16. The XRD pattern is consistent with the standard card of monoclinic $\text{VO}_2(\text{M})$ (JCPDS Card No. 82-0661), giving the pure phase nature of the as-prepared $\text{VO}_2(\text{M})$ submicrospheres.

S7-4. DSC curve of the as-prepared $\text{VO}_2(\text{M})$ hollow submicrospheres

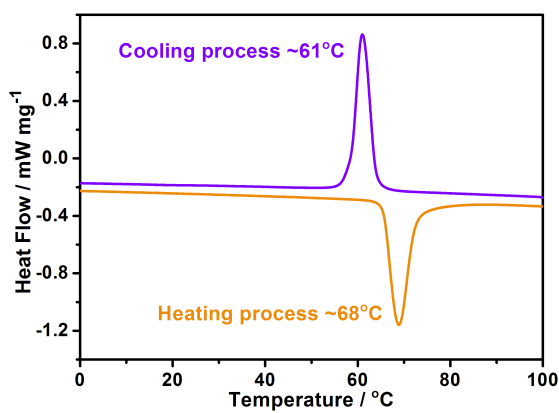


Figure S17. DSC curve ranging from 0 °C to 100 °C of the as-prepared $\text{VO}_2(\text{M})$ hollow submicrospheres shows a remarkable phase transition at ~68 °C for heating process and ~61 °C for cooling process, which is consistent with the phase change behavior of monoclinic $\text{VO}_2(\text{M})$.

S7-5. HRTEM image of $\text{VO}_2(\text{M})$ hollow submicrospheres

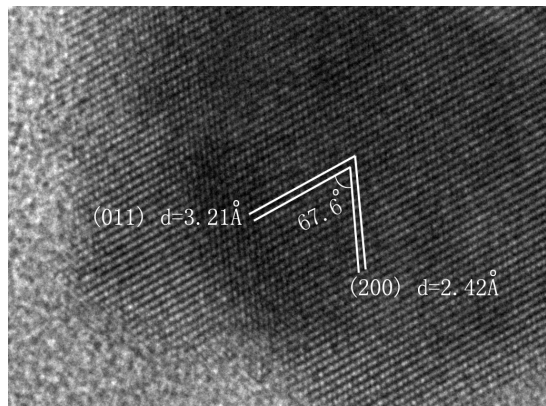


Figure S18. HRTEM image of the $\text{VO}_2(\text{M})$ hollow submicrospheres revealed the pure phase nature of the sample. It is obvious that the $\text{VO}_2(\text{M})$ submicrospheres are of good crystallinity with less grain boundaries than the GBR- $\text{VO}_2(\text{R})$ as a result of the long-time calcination.

S7-6. Preparation details of $\text{VO}_2(\text{R})$, $\text{VO}_2(\text{B})$, $\text{VO}_2(\text{M})$, $\text{VO}_2(\text{P})$ and V_2O_5

$\text{VO}_2(\text{R})$: Bulk $\text{VO}_2(\text{R})$ was synthesized according to our previously reported literature.^[7]

$\text{VO}_2(\text{B})$: 510 mg vanadium pentoxide (V_2O_5) and 450 mg oxalic acid ($\text{H}_2\text{C}_2\text{O}_4$) were dispersed in 40 mL distilled water. After vigorous stirring for 10 min, the suspension was transferred into a 50 mL Teflon-lined stainless steel autoclave and maintained at 200 °C for 2 days. The autoclave was cooled to room temperature naturally. The as-obtained dark green precipitate was washed with distilled water and ethanol for several times and dried at 60 °C under vacuum.

$\text{VO}_2(\text{M})$: Bulk $\text{VO}_2(\text{M})$ was obtained by heating the as-prepared $\text{VO}_2(\text{B})$ at 700 °C for 4 h in nitrogen atmosphere.

$\text{VO}_2(\text{P})$: $\text{VO}_2(\text{P})$ nanostructures were synthesized via a method we reported in earlier literature.^[8]

V_2O_5 : V_2O_5 was obtained from commercial route and used without further purification.

$\text{VO}_2(\text{M})$ hollow submicrospheres: $\text{VO}_2(\text{M})$ hollow submicrospheres was obtained by heating nsutite-type VO_2 hollow nanoarchitectures at 350 °C for 48 h in nitrogen atmosphere.

All the samples were degassed at 200 °C before taking the BET measurement and hydrogen uptake experiments.

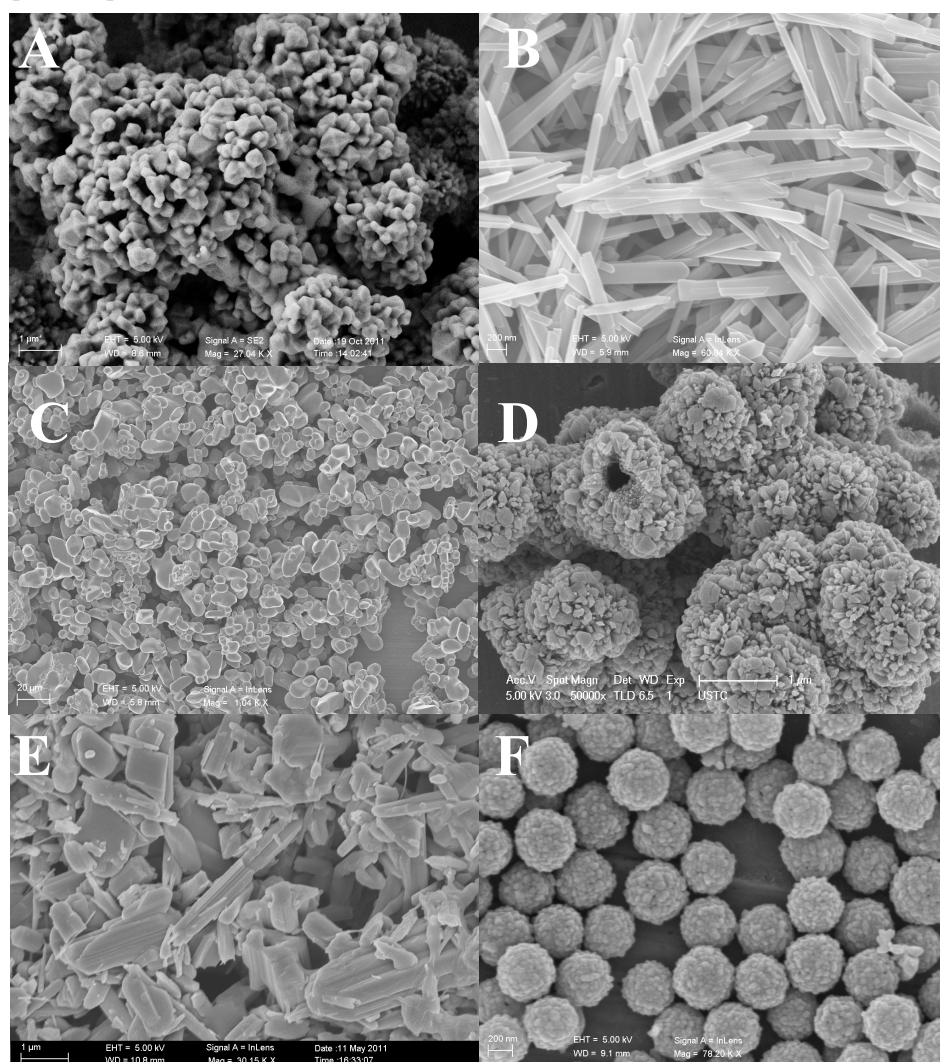


Figure S19. SEM images of (A) Bulk rutile $\text{VO}_2(\text{R})$, (B) $\text{VO}_2(\text{B})$ nanorods, (C) $\text{VO}_2(\text{M})$ bulk, (D) $\text{VO}_2(\text{P})$ nanostructures, (E) V_2O_5 and (F) $\text{VO}_2(\text{M})$ hollow submicrospheres for A-E respectively.

References in Electronic Supplementary Information

- [1] P.E. Blöchl, *Phys. Rev. B* 1994, **50**, 17953.
- [2] J.P. Perdew, K. Burke, M. Ernzerhof, *Phys. Rev. Lett.* 1996, **77**, 3865.
- [3] J. Heyd, G.E. Scuseria, M. Ernzerhof, *J. Chem. Phys.* 2003, **118**, 8207; Erratum: *J. Chem. Phys.* 2006, **124**, 219906.
- [4] G. Kresse, J. Hafner, *Phys. Rev. B* 1993, **48**, 13115.
- [5] G. Kresse, J. Furthmüller, *Phys. Rev. B* 1996, **54**, 11169.
- [6] G. Kresse, D. Joubert, *Phys. Rev. B* 1999, **59**, 1758.
- [7] C. Wu, F. Feng, J. Feng, J. Dai, L. Peng, J. Zhao, J. Yang, C. Si, Z. Wu, Y. Xie, *J. Am. Chem. Soc.*, 2011, 133, 13798.
- [8] C. Wu, F. Feng, J. Feng, J. Dai, J. Yang, Y. Xie, *J. Phys. Chem. C* 2010, **115**, 791.